

# Dislocation Configurations in an Extruded ZK60 Magnesium Alloy

B. LI, E. MA, and K.T. RAMESH

Transmission electron microscopy (TEM) was performed to study the types of dislocations and their configurations in a commercially extruded ZK60 magnesium (Mg) alloy. We mainly employed the weak-beam dark-field (WBDF) technique with  $\langle 01\bar{1}0 \rangle$  zone axis to unambiguously identify Burgers vectors of various types of dislocations in the microstructure. It was found that nonbasal  $\langle a \rangle$  dislocations and  $\langle c \rangle$  dislocations were predominant. No  $\langle c + a \rangle$  was observed. Rearrangement of these dislocations, due to dynamic recovery during extrusion, led to cell walls and low-angle grain boundaries with relatively high density dislocations. Dissociation of the  $\langle c \rangle$  dislocations with a relatively narrow split distance was observed. The dissociated  $\langle c \rangle$  dislocations could form a nodular structure. Fringes of stacking faults from the dislocation dissociation were observed.

DOI: 10.1007/s11661-008-9621-3

© The Minerals, Metals & Materials Society and ASM International 2008

## I. INTRODUCTION

IN recent years, magnesium (Mg) and Mg-based alloys have drawn significant attention as attractive lightweight alloys. Among them, the family of ZK60 Mg alloys (based on Mg-6.0Zn-0.5Zr) is of great interest,<sup>[1–3]</sup> because these alloys possess relatively high strength (compared to other Mg alloys) and ductility. Extruded ZK60 alloys<sup>[1,4–6]</sup> have also been used as the starting material for severe plastic deformation using, for example, equal channel angular extrusion (ECAE). This processing route that involves heavy plastic deformation is related to the ongoing efforts to improve the mechanical properties of alloys by reducing the grain size down to the ultrafine grain and even nanocrystalline range.<sup>[7–16]</sup>

Despite the extensive investigation on extruded ZK60 alloys, their dislocation structure remains unclear. Extrusion is an important industrial practice to refine the grain structure in Mg and Mg alloys. It can be expected that during extrusion to high strains, the microstructure of the ZK60 alloys experiences drastic changes in terms of the generation of defect structures such as various types of dislocations, twins, and stacking faults. The resultant mechanical properties, such as the strength of the extruded alloys, obviously strongly depend on the dislocations and their configurations in the microstructure. This makes a systematic investigation of the types and configurations of dislocation in extruded ZK60 important for building the foundation for understanding further dislocation evolution in subsequent deformation (*e.g.*, in shaping or mechanical

tests), and for comparisons with the dislocations developed in other processing routes such as ECAE.

From the perspective of fundamental research, dislocation slips in hcp Mg and Mg alloys are also of interest, especially because they are much less understood than those in fcc and bcc metals. In-depth analyses of dislocations and dislocation configurations in extruded ZK60 are particularly lacking, probably due to the following reasons. First, dislocation structures of the hcp crystals are rather complex and prior data are often contradictory. The hcp Mg has three operative dislocation Burgers vectors:<sup>[17]</sup>  $\langle a \rangle = \frac{1}{3}\langle 11\bar{2}0 \rangle$ ,  $\langle c \rangle = [0001]$ , and  $\langle c + a \rangle = \frac{1}{3}\langle 11\bar{2}3 \rangle$ . Depending on the temperature at which the material is plastically deformed, and the crystallographic orientation in which the material is loaded, these three Burgers vectors are all possible. For  $\langle a \rangle$  dislocations, the slip systems can be basal or prismatic. For  $\langle c + a \rangle$  dislocations, the slip plane possibly can be on the major twinning planes such as  $\{10\bar{1}1\}$ ,  $\{11\bar{2}1\}$ , or  $\{11\bar{2}2\}$ . These facts make the determination of dislocation identities non-trivial. As a result, there have been controversies for defect structures in Mg alloys. Second, preparation of clean, electron transparent specimens is rather difficult, because Mg is so reactive that oxidation and contamination can be easily introduced during a specimen preparation process such as electropolishing.

A definitive investigation on the dislocation structures in extruded ZK60 alloys is also very important for modeling of texture development during grain refining processes. Low symmetry hcp materials have a strong propensity for texturing during processing such as rolling, extrusion, and ECAE. Recently, texture has been a major topic for the mechanical properties of hcp materials.<sup>[18–21]</sup> Dislocation slip has been considered as an important contribution to the formation of texture, in addition to mechanical twinning.<sup>[22–24]</sup> To validate and refine theoretical models, identifying the dislocations with clarity becomes crucial.

---

B. LI, Postdoctoral Fellow, E. MA and K.T. RAMESH, Professors, are with the Center for Advanced Metallic and Ceramic Systems, Johns Hopkins University, Baltimore, MD 21218. Contact e-mail: bli@jhu.edu

Manuscript submitted January 7, 2008.

Article published online August 20, 2008

In the following, we present the results of a transmission electron microscopy (TEM) study of an as-received ZK60 Mg alloy, which has been extruded using a commercial process. Our goal is to identify what types of dislocations are present and how they are rearranged inside the microstructure.

## II. EXPERIMENTAL

The material used in this work was a slab of extruded ZK60 Mg alloy obtained from a commercial supplier (metalmarket.com). The temperature and area reduction ratio for commercial extrusion of ZK60 are around 360 °C (633 K) and 18, respectively. A sample of 600  $\mu\text{m}$  in thickness was cut off perpendicular to the extrusion direction by electrical discharge machining, and then polished down to about 130  $\mu\text{m}$  using a series of sand papers down to 800 grit. Water has to be avoided during final polishing to reduce corrosion. The 3-mm discs were then mechanically punched off the sample. The TEM specimens were polished using a Tenupol-3 electropolisher (Struers, Westlake, OH) with a perchloric (<2 pct) ethanol solution. Afterward, the specimens were cleaned by ion milling for about 0.5 hours with liquid nitrogen cooling using very gentle milling conditions (low incidental angle and low voltage). The TEM observations were then carried out on a PHILIPS\* 420 microscope

---

\*PHILIPS is a trademark of Philips Electronics Instruments Corp., Mahwah, NJ.

---

with a double-tilt specimen stage. The accelerating voltage was 120 kV.

## III. RESULTS AND ANALYSES

The average grain size of the as-received extruded ZK60 alloy was about 2 to 3  $\mu\text{m}$  from the TEM examinations. Twins were seen occasionally under TEM (those that were not at the proper diffraction conditions would not be visible). An example is shown in Figure 1 for a grain that is relatively large compared with the average size. Twins are seen to run across the grain boundaries and extend to the neighboring grains. Also, some twin plates are broken into fragments during extrusion. Because our focus here is on dislocations, in the following text, we will not discuss in detail the twinning activities.

To observe the dislocations, the specimen was tilted to the  $\langle 11\bar{2}0 \rangle$  zone axis. The typical microstructure is shown in Figure 2, where a relatively large grain is subdivided into domains of 1 to 2  $\mu\text{m}$  in size, separated by subgrain boundaries. This figure indicates that during extrusion, a large population of subgrain boundaries was developed as a result of the rearrangement of dislocations generated during heavy plastic deformation. These low-angle boundaries are dislocation walls composed of a high density of dislocations, as discussed next.

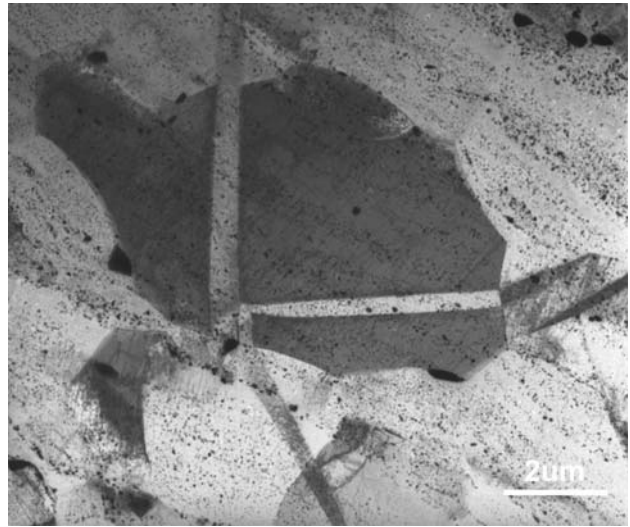


Fig. 1—Grain structure in a commercially extruded ZK60 Mg alloy. Twins are observed occasionally, some of which run across grain boundaries.

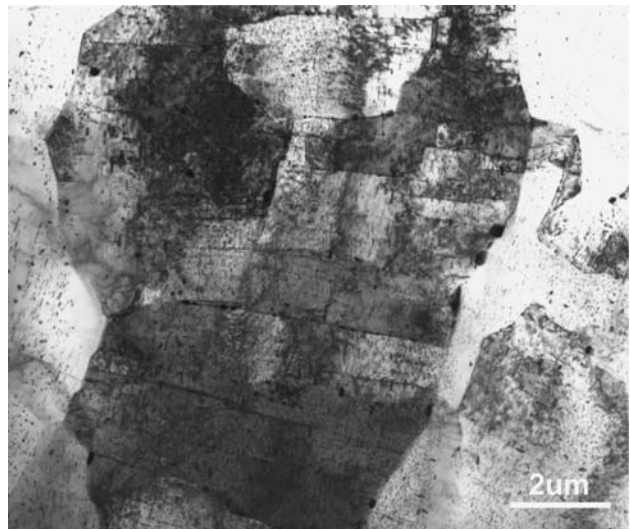


Fig. 2—When the specimen was tilted to zone axis  $\langle 11\bar{2}0 \rangle$ , subgrain boundaries inside grains can be seen at low magnification. This structure is typical in the grains of the extruded ZK60 alloy. The size of the domains is on the order of 1.0 to 2.0  $\mu\text{m}$ .

The dislocation walls are studied at higher magnifications, as shown, for example, in Figure 3. One type of dislocation contrast in Figure 3(a) is the vertical lines, which will be discussed in Section IV. The other type of contrast is the bold, kinky lines running from left to right (indicated by the vertical arrows in Figure 3(a)). These line segments are dislocation walls that form low-angle grain boundaries, as shown in Figure 3(b) with higher magnification. Individual dislocations in such a low-angle grain boundary can be seen in Figure 3(c). The pattern in which the dislocations are arranged suggests that these dislocations are in the prism planes, because the angles between the segments exactly coincide with the geometry of the prism planes in the hcp crystal structure.



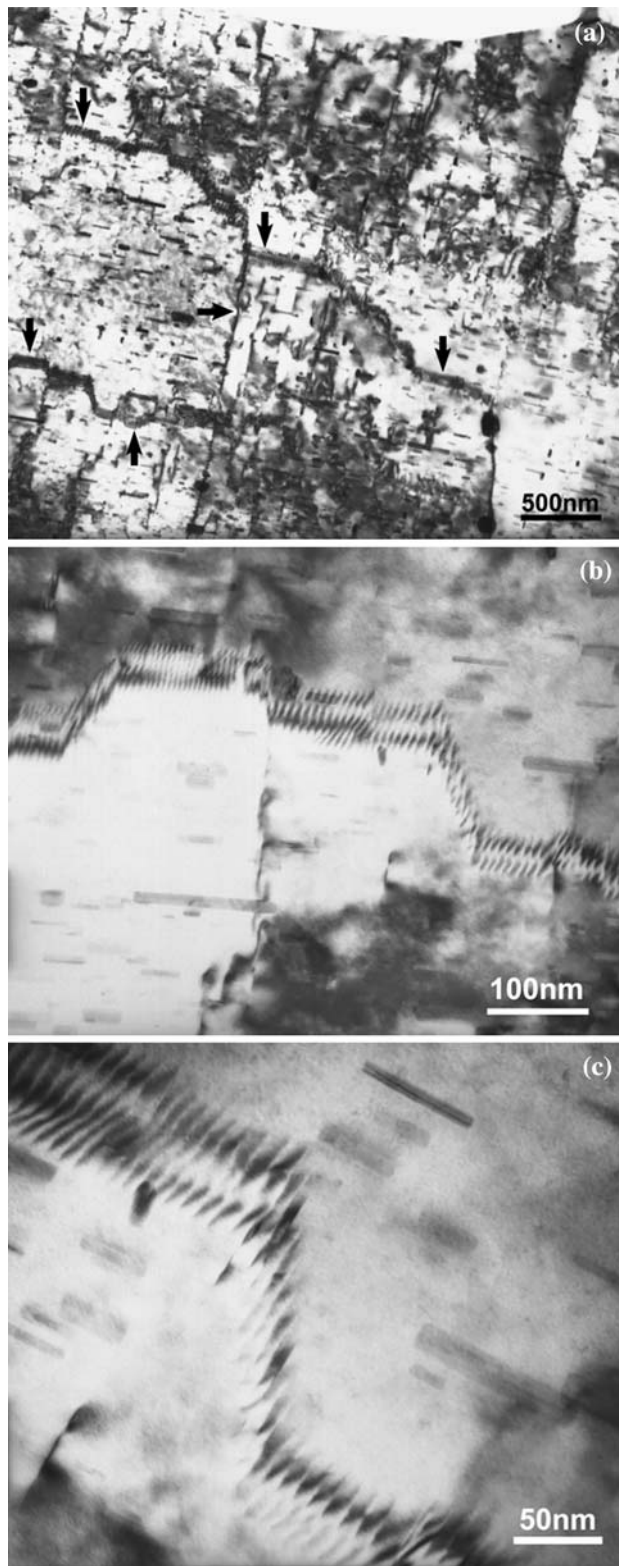


Fig. 3—Dislocation walls inside a grain. (a) The dislocation wall can almost run through a grain (the bold, kinky, dark lines marked by the vertical arrows running from left to right). The horizontal arrow indicates another type of dislocation contrast (vertical lines). The details of the kinky dislocation wall can be better resolved at (b) and (c) high and higher magnifications. In (c), contrast of the strain field of the individual dislocations can be seen. The pattern that the dislocations were arranged indicates that the dislocation slip has to be in the prism planes. Rodlike precipitates were observed as well.

Figure 4 shows how dislocations are organized into low-angle grain boundaries. In Figure 4(a), a subgrain is bounded by dislocation walls, which is typical in the extruded ZK60. Figure 4(b) shows the intersection of arrays of dislocations. The comparatively narrower, horizontal dislocation lines seen here are identical to those vertical lines in Figure 3(a) (marked by the horizontal arrow). Figure 4(c) shows the dislocations lying in a different slip plane: the dislocation contrast looks different, but the dislocations actually have the same Burgers vector as in Figures 4(a) and (b). The dislocation walls can also present very different contrasts at different zone axes. In Figure 4(d), where the zone axis was tilted to  $\langle 01\bar{1}0 \rangle$ , the low-angle grain boundary is still composed of a high density of dislocations, but the individual dislocations can hardly be seen in the bright-field (BF) imaging.

In addition to the dislocations, rod-shaped precipitates can be seen. These precipitates are MgM (M = Zn, Zr) intermetallics, according to energy dispersive X-ray spectroscopy characterization by Watanabe *et al.*<sup>[25]</sup>

Figure 5 shows the dissociation of a dislocation. The split width is narrow, suggesting a relatively high stacking fault energy (SFE). Interestingly, the dissociated dislocations periodically rejoin together, forming a nodular structure, as indicated by the arrow in Figure 5. These long, twisted dislocation lines are actually those vertical lines observed at lower magnification in Figure 3(a).

To identify the Burgers vector of the dislocations in an hcp structure, specific reflections have to be used to better distinguish the dislocations. There are three possible Burgers vectors,  $\langle a \rangle$ ,  $\langle c \rangle$ , and  $\langle c + a \rangle$ , and there are a total of three types of  $\langle a \rangle$  Burgers vectors and six types of  $\langle c + a \rangle$  Burgers vectors. Therefore, tilting and selecting particular reflections at a specific zone axis becomes very important in characterizing the Burgers vectors. For example, the Burgers vector of type  $\langle a \rangle$  dislocation is perpendicular to that of  $\langle c \rangle$  dislocations; thus, we can use 0002 and  $2\bar{1}10$  reflections to image and differentiate these dislocations. However, the magnitude of the Burgers vectors of the  $\langle c \rangle$  dislocations is 62 pct larger than that of the  $\langle a \rangle$  dislocations, and the strain field of the  $\langle a \rangle$  dislocations can be overwhelmed by the  $\langle c \rangle$  dislocations. As a result, a lot of  $\langle a \rangle$  dislocations cannot be seen in BF images even though the Bragg condition is satisfied. On the other hand, the much larger Burgers vector of the  $\langle c \rangle$  dislocations makes these dislocations remain visible even though the visibility criterion is not satisfied, leading to possible misinterpretation of  $\langle c \rangle$  as  $\langle c + a \rangle$  in BF imaging. Hence, the weak-beam dark-field (WBDF) technique is preferred to identify the dislocations with clarity.

Figure 6 shows a comparison between the strong-beam BF and WBDF imaging and demonstrates that WBDF is preferred in the analyses of dislocation structure in hcp Mg and Mg alloys. In Figure 6(a), a two-beam condition was set up and a BF image was taken with  $\bar{2}110$  reflection. The dislocation wall composed of  $\langle c \rangle$  dislocations (marked by the arrow) is invisible (the contrast is sufficiently low or  $g \cdot b$  is small) as expected, but so are the  $\langle a \rangle$  dislocations, which are

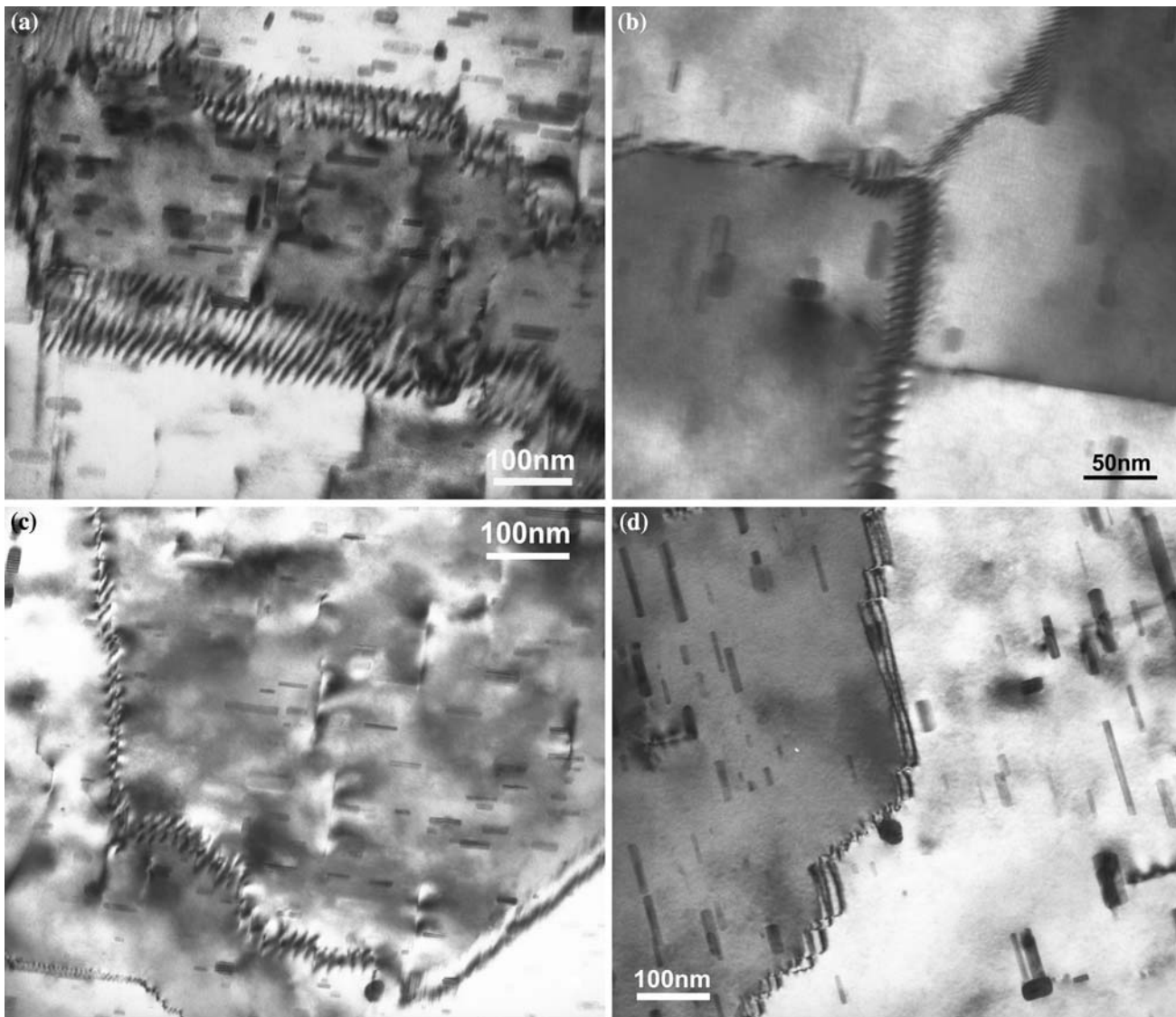


Fig. 4—Low-angle grain boundaries made up of dislocations walls. (a) A subgrain was bounded by dislocations. (b) Interaction between dislocation configurations. Nodular dislocations intercept with a low-angle grain boundary. (c) Low-angle grain boundaries, where dislocations have the same Burgers vectors as in (a) and (b), but on different prismatic slip plane. (d) When tilted to the  $\langle 01\bar{1}0 \rangle$  zone axis, the dislocation walls present different contrast, and individual dislocation can hardly be seen.

expected to be visible. In the WBDF image (Figure 6(b)) with the same reflection, the  $\langle c \rangle$  dislocations completely disappear, but the  $\langle a \rangle$  dislocations are visible (marked by the arrows). We therefore mainly applied the WBDF technique in the contrast analyses. In these operations, two-beam conditions were set up before taking the WBDF images. In most cases, the specimen was tilted to the  $\langle 01\bar{1}0 \rangle$  zone axis by following the Kikuchi pattern, where only reflections from  $11\bar{2}0$  and  $0002$  and their combinations were present. These two particular reflections were then used to identify  $\langle a \rangle$  and  $\langle c \rangle$  dislocations with WBDF. If there are  $\langle c + a \rangle$  dislocations present, they should appear in images of both reflections. Such a one-to-one correspondence makes the contrast analyses unambiguous. Diffraction patterns at the  $\langle 01\bar{1}0 \rangle$  zone axis were provided as insets in the micrographs, whereas the two-beam patterns were not shown.

Figure 7 shows an example of determining the Burgers vectors using  $0002$  and  $2\bar{1}\bar{1}0$  reflections with zone axis  $\langle 01\bar{1}0 \rangle$ . The contrast criterion  $g \cdot b = 0$  worked very well for the  $\langle c \rangle$  and  $\langle a \rangle$  dislocations in the WBDF images. In Figure 7(a), only  $\langle c \rangle$  dislocations can be seen from reflection  $0002$ . When the specimen was tilted to  $2\bar{1}\bar{1}0$ , all the  $\langle c \rangle$  dislocations disappeared, but  $\langle a \rangle$  dislocations appeared. No dislocations can be seen in both reflections, indicating that no  $\langle c + a \rangle$  dislocations were present.

In the WBDF image of Figure 8(a),  $\langle a \rangle$  dislocations were rearranged into a low-angle grain boundary. In addition, short, nonrectilinear  $\langle a \rangle$  dislocations and small loops with high density can be seen in the background (an example is marked by the arrow). These dislocations were difficult to see in BF images. In Figure 8(b), dislocation pileup and low-angle grain boundaries



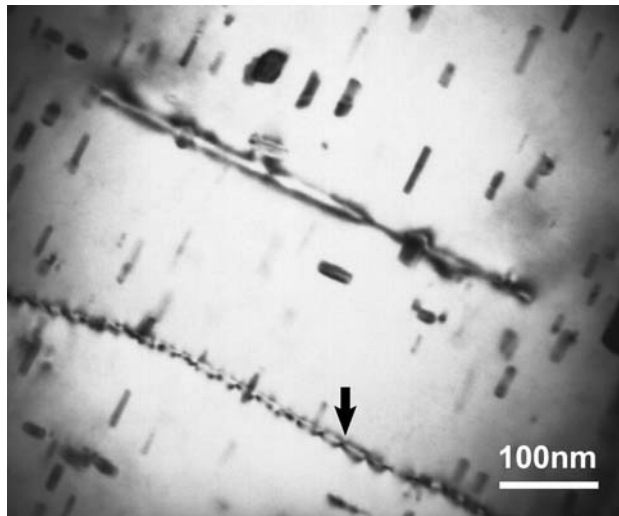


Fig. 5—Dissociation of dislocations. The split width is narrow. The dissociated dislocations can join together and form a nodular structure (indicated by the arrow), such that the dislocation line appears twisted.

composed of  $\langle c \rangle$  dislocations can be seen (marked by the arrows).

As we have seen from Figure 5, dislocation split was observed. The contrast analyses show that the dislocations in Figure 5 are all  $\langle c \rangle$  dislocations without  $\langle a \rangle$  component. The split width is narrow. The SF between the partial dislocations, however, cannot be seen in Figure 5. When the dissociated  $\langle c \rangle$  dislocations are rearranged into a low-angle grain boundary, the contrast of the stacking fault can be observed at some specific zone axis, as shown in Figure 9. The split of the  $\langle c \rangle$  dislocations can be seen in the WBDF image (Figure 9(a)), where each dislocation line splits slightly into two partials (the inset). When the specimen was tilted to the  $\langle 11\bar{2}0 \rangle$  zone axis, fringes from the SFs with the dislocation lines can be clearly seen. Figure 9(c) shows that high density  $\langle c \rangle$  dislocations were rearranged into a low-angle grain boundary. At the imaging zone axis  $\langle 01\bar{1}0 \rangle$ , no SFs can be seen. When the specimen was tilted to zone axis  $\langle 11\bar{2}0 \rangle$ , the contrast of the SFs emerged.

The dislocations in Figures 3 and 4 are all  $\langle c \rangle$  dislocations. All of the dislocations observed in this work are in the prism planes. Basal  $\langle a \rangle$  dislocations were hardly observed, and neither were the  $\langle c + a \rangle$  dislocations.

#### IV. DISCUSSION

The TEM study in this work demonstrates that during extrusion of ZK60 Mg alloy, a high density of dislocations were generated and rearranged into subgrain boundaries. The dislocations were found to be mainly  $\langle a \rangle$  and  $\langle c \rangle$  types on the prism planes. Basal  $\langle a \rangle$  and pyramidal  $\langle c + a \rangle$  dislocations were hardly observed.

Dislocations in Mg and Mg alloys have been investigated previously by a number of researchers.<sup>[26–28]</sup> In general, at low temperatures and at the initiation of

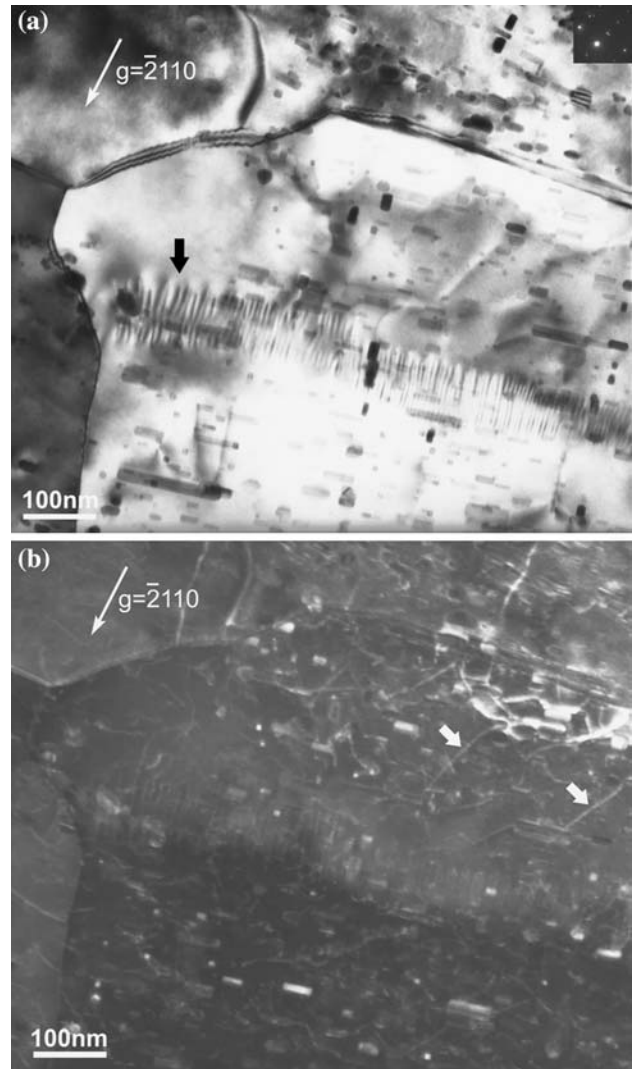


Fig. 6—Comparison between (a) strong-beam BF image and (b) WBDF. In (b), all the  $\langle c \rangle$  dislocations of the dislocation wall (indicated by arrow) completely disappeared and the presence of  $\langle a \rangle$  dislocations became clear (marked by arrows) as opposed to being invisible in (a), though the same reflection was used in both cases. The inset is the recorded diffraction pattern at the zone axis.

plastic deformation, basal  $\langle a \rangle$  slip was considered to be the dominant mechanism,<sup>[26]</sup> presumably because basal  $\langle a \rangle$  slip has a low critical resolved shear stress. However, basal  $\langle a \rangle$  dislocations alone cannot satisfy the von-Mises criterion. Also,  $\langle a \rangle$  dislocations (both basal and prismatic) cannot accommodate the plastic strain along the  $\langle c \rangle$  axis. Hence, nonbasal dislocations such as prismatic and pyramidal  $\langle c + a \rangle$  dislocations are activated as a result of high compatibility stresses at grain boundaries,<sup>[29]</sup> cross-slip of basal  $\langle a \rangle$  dislocations to prism planes, and then to pyramidal planes.<sup>[28]</sup> Such cross-slip may require the dissociated basal  $\langle a \rangle$  dislocations to recombine before cross-slip can happen.<sup>[26]</sup>

A significant amount of effort has been made to explore the dislocation structure of the pyramidal  $\langle c + a \rangle$  slip in hcp crystals, but it is less understood in Mg and Mg alloys.<sup>[30–32]</sup> Several models were proposed

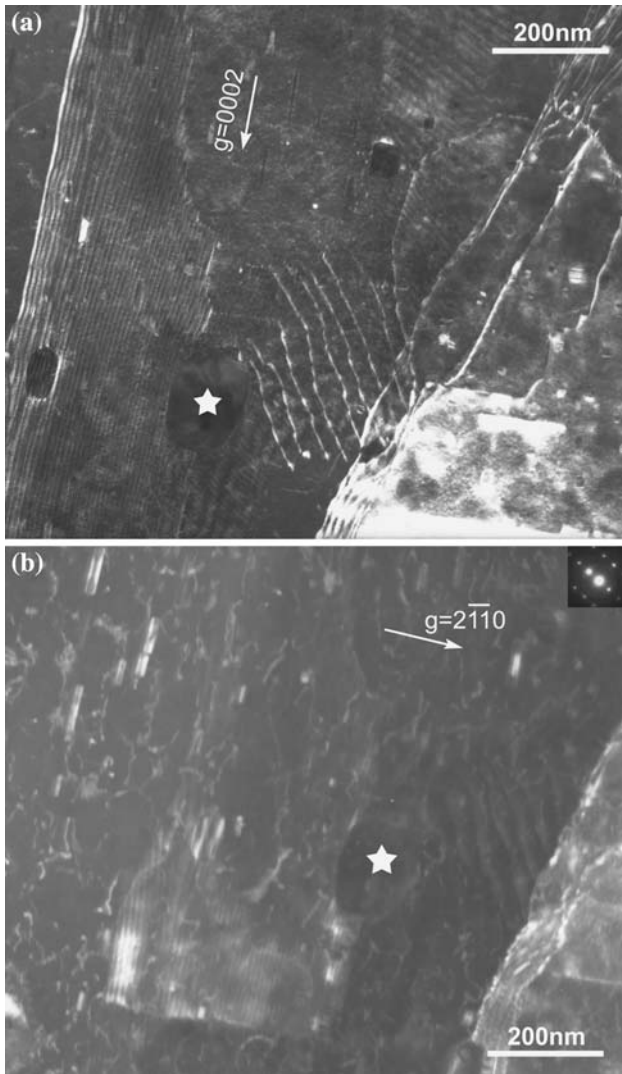


Fig. 7—(a) and (b) WBDF images of the dislocations by using 0002 and  $2\bar{1}10$  reflections at the zone axis  $\langle 01\bar{1}0 \rangle$ . Many  $\langle c \rangle$  dislocations are visible near the star in (a) but disappear in (b), whereas the  $\langle a \rangle$  dislocations appeared in (b) but not in (a). A precipitate is marked with a star for reference. The inset is the recorded diffraction pattern at the zone axis.

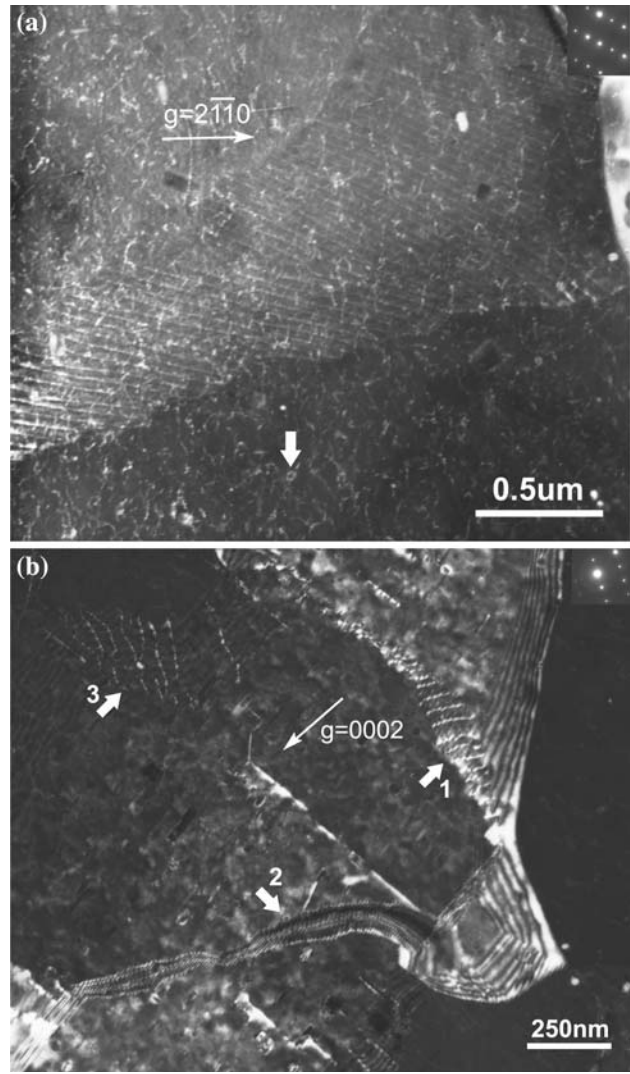


Fig. 8—(a) WBDF image of dislocations with  $\langle a \rangle$  Burgers vector. Note the high density, nonrectilinear dislocations and loops in the background (marked by the arrow). (b) Dislocation pileup (location 3) and low-angle grain boundaries (location 1 and 2) composed of  $\langle c \rangle$  dislocations (indicated by the arrows). The inset is the recorded diffraction pattern at the zone axis.

to describe the possible dissociation of the  $\langle c + a \rangle$  dislocations,<sup>[30–32]</sup> but so far only the  $\langle c + a \rangle \rightarrow \langle c \rangle + \langle a \rangle$  split was observed<sup>[33]</sup> by TEM (no stacking fault was observed in previous work, however). All the molecular dynamics simulations predicting the core structure and the SFs of the pyramidal slip in Mg<sup>[30–32]</sup> show that the  $\langle c + a \rangle$  dislocations must be unstable due to the exceptionally large Burgers vector (91 pct larger than  $\langle a \rangle$ ), and they most likely dissociate into partials. Hence, presumably,  $\langle c \rangle$  and  $\langle a \rangle$  dislocations can be considered as a consequence of dissociation of  $\langle c + a \rangle$  pyramidal dislocations.<sup>[26,33]</sup> However, traces of  $\langle c + a \rangle$  dislocations were hardly observed in this work, and this does not support the finding that the high density  $\langle c \rangle$  and nonbasal  $\langle a \rangle$  dislocations were generated mainly as the product of the dissociation of the  $\langle c + a \rangle$  pyramidal dislocations.

Previous investigations suggest that nonbasal slips in Mg and Mg alloys are strongly temperature dependent.<sup>[33,34]</sup> Galiyev *et al.*<sup>[34]</sup> studied the deformation mechanisms of ZK60 alloy at different temperatures and showed that below 423 K, activities of basal  $\langle a \rangle$  dislocations are significant. As the temperature is increased, dislocation densities from both basal  $\langle a \rangle$  and  $\langle c + a \rangle$  slip notably decrease. The zone axes ( $\langle 11\bar{2}0 \rangle$  and  $\langle 01\bar{1}0 \rangle$ ) used in imaging the dislocations in this work are all contained in the basal plane, and the contrast of basal  $\langle a \rangle$  dislocations should be present readily if such dislocations are present.<sup>[26]</sup> It is likely that because the temperatures for commercial extrusion are relatively high, the basal and  $\langle c + a \rangle$  slips in our samples are annihilated. Hence, the temperature dependence may explain the observations in the extruded ZK60.



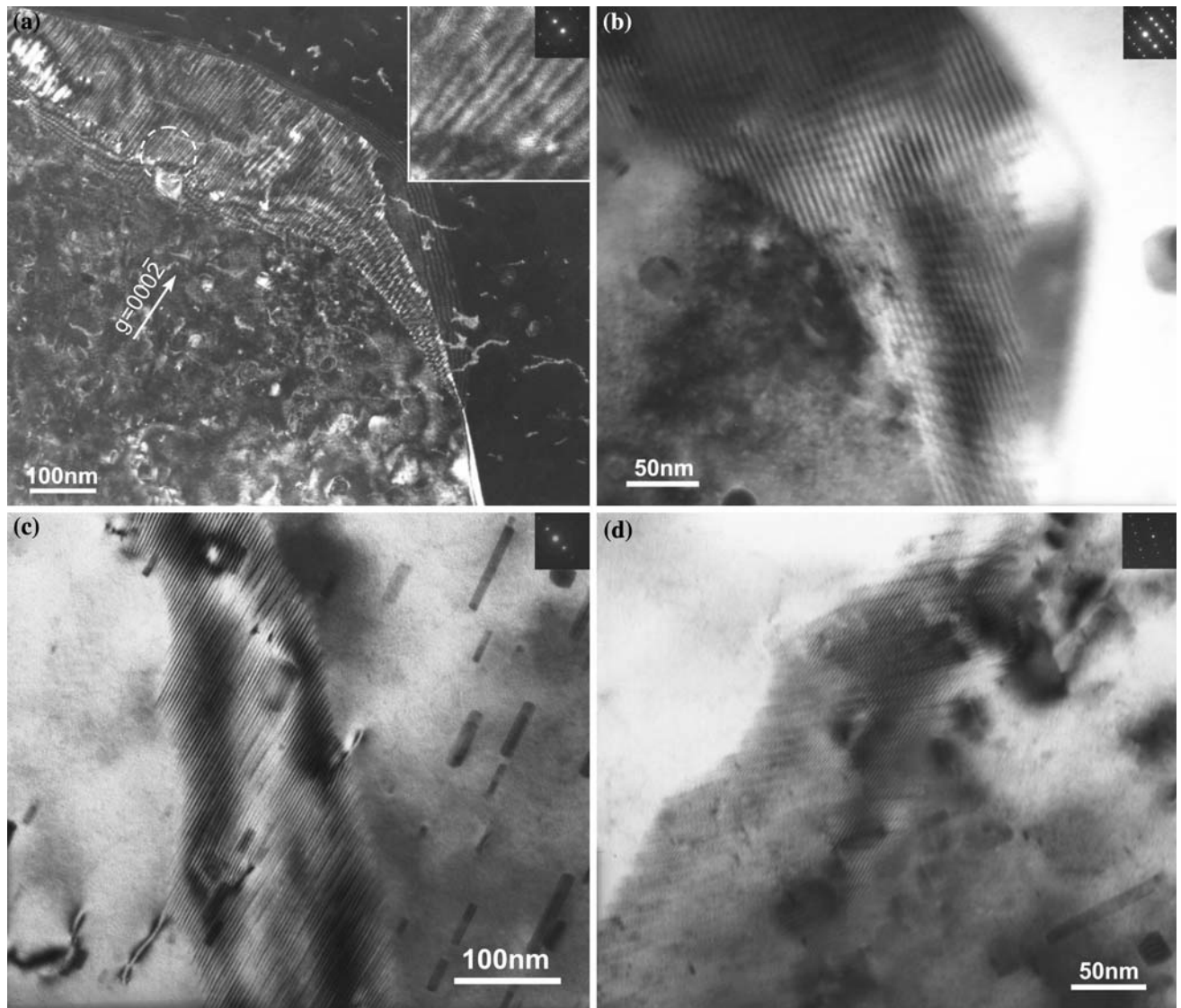


Fig. 9—Contrast from the stacking faults from the split of  $\langle c \rangle$  dislocations. (a)  $\langle c \rangle$  dislocation wall. The individual  $\langle c \rangle$  dislocations dissociate narrowly, as shown in the inset (blowup from the circled area). (b) The same area as in (a); fringes of SFs can be seen when tilted to the  $\langle 11\bar{2}0 \rangle$  zone axis. The fringes of the SFs overlap with the  $\langle c \rangle$  dislocations. (c) A dislocation wall composed of  $\langle c \rangle$  dislocations. (d) The same area as in (c); fringes of SFs can be seen at the  $\langle 11\bar{2}0 \rangle$  zone axis.

The nonbasal dislocations observed in this work were rearranged into pileups, cell boundaries, and low-angle boundaries during the rather heavy plastic deformation at an elevated temperature, indicating dynamic recovery occurred during processing. The mechanism for dislocation rearrangement during plastic flow was described previously by the “dislocation percolation model,”<sup>[35]</sup> where interaction between moving dislocations and randomly distributed stopping obstacles such as solute atoms, secondary phases, forest dislocations, etc. produces local dislocation storage in “hard” regions and dislocation penetration in “soft” regions in the slip planes. The dislocations stored eventually evolve into cell structures under the action of forward stress inside the dislocation loops. Aided by the elevated temperature, the cell structure and dislocation tangles could further evolve into low-angle grain boundaries.

Direct TEM observation of the dissociation of  $\langle c \rangle$  dislocations and the resultant SFs has not been reported in previous work. The  $\langle c \rangle$  dislocations, which have a Burgers vector 62 pct larger than  $\langle a \rangle$  dislocations, are presumably energetically unstable. To better understand the split of the  $\langle c \rangle$  dislocations and the resultant SF, molecular dynamics simulations will be performed to calculate the generalized SFE,<sup>[36]</sup> and the results will be reported in future publications.

## V. CONCLUSIONS

We have attempted WBDF imaging and successfully identified the dislocation structure and configurations in commercially extruded ZK60 Mg alloy. Nonbasal  $\langle a \rangle$  dislocations and  $\langle c \rangle$  dislocations are found to be

predominant, whereas basal  $\langle a \rangle$  and pyramidal  $\langle c + a \rangle$  dislocations were hardly observed, for the particular extrusion temperature (360 °C) and straining conditions.

The nonbasal  $\langle a \rangle$  and the  $\langle c \rangle$  dislocations were rearranged into cell walls and low-angle grain boundaries during extrusion, indicating that dynamic recovery occurred during extrusion. Dissociation of the  $\langle c \rangle$  dislocations was observed, and the split width was narrow. The dissociated  $\langle c \rangle$  dislocations were rearranged into nodular structures and low-angle boundaries. Fringes due to the stacking faults were seen when the specimen was tilted to certain specific orientations.

## ACKNOWLEDGMENTS

The authors are grateful to Dr. K. Livi for his technical assistance with the TEM work and K. Azevedo and Dr. D. Elbert for their help with sample preparation. This work is supported at the Center for Advanced Metallic and Ceramic Systems (CAMCS) by ARMAC-RTP, DAAD19-01-2-0003, and W911NF-06-2-0006.

## REFERENCES

1. H. Somekawa and T. Mukai: *Mater. Trans. JIM*, 2006, vol. 47, pp. 995–998.
2. R. Lapovok, P.F. Thomson, R. Cottam, and Y. Estrin: *Mater. Trans. JIM*, 2004, vol. 45, pp. 2192–99.
3. H. Watanabe, T. Mukai, K. Ishikawa, and K. Higashi: *Scripta Mater.*, 2006, vol. 46, pp. 851–56.
4. K. Furuno, H. Akamatsu, K. Oh-ishi, M. Furukawa, Z. Horita, and T.G. Langdon: *Acta Mater.*, 2004, vol. 52, pp. 2497–2507.
5. M. Furui, H. Kitamura, H. Anada, and T.G. Langdon: *Acta Mater.*, 2007, vol. 55, pp. 1083–91.
6. R.B. Giguireredo and T.G. Langdon: *Mater. Sci. Eng.*, 2006, vol. 430A, pp. 151–56.
7. R.Z. Valiev and T.G. Langdon: *Progr. Mater. Sci.*, 2006, vol. 51, pp. 881–981.
8. D. Jia, Y. Wang, K.T. Ramesh, E. Ma, Y.T. Zhu, and R. Valiev: *Appl. Phys. Lett.*, 2001, vol. 79, pp. 611–13.
9. Y.M. Wang, E. Ma, R.Z. Valiev, and Y.T. Zhu: *Adv. Mater.*, 2004, vol. 16, pp. 328–31.
10. A. Yamashita, Z. Horita, and T.G. Langdon: *Mater. Sci. Eng.*, 2001, vol. A300, pp. 142–47.
11. K. Matsubara, Y. Miyahara, Z. Horita, and T.G. Langdon: *Acta Mater.*, 2003, vol. 51, pp. 3073–84.
12. K. Furuno, H. Akamatsu, K. Oh-ishi, M. Furukawa, Z. Horita, and T.G. Langdon: *Acta Mater.*, 2004, vol. 52, pp. 2497–2507.
13. M. Furui, H. Kitamura, H. Anada, and T.G. Langdon: *Acta Mater.*, 2007, vol. 55, pp. 1083–91.
14. R.B. Giguireredo and T.G. Langdon: *Mater. Sci. Eng.*, 2006, vol. 430A, pp. 151–56.
15. R.B. Figureiredo, P.R. Cetlin, and T.G. Langdon: *Acta Mater.*, 2007, vol. 55, pp. 4769–79.
16. H.Q. Sun, Y.-N. Shi, M.-X. Zhang, and K. Lu: *Acta Mater.*, 2007, vol. 55, pp. 975–82.
17. D.J. Bacon and V. Vitek: *Metall. Mater. Trans. A*, 2002, vol. 33A, pp. 721–33.
18. J. Bohlen, M.R. Nurnberg, J.W. Senn, D. Letzig, and S.R. Agnew: *Acta Mater.*, 2007, vol. 55, pp. 2101–12.
19. S.R. Agnew, P. Mehrotra, T.M. Lillo, G.M. Stoica, and P.K. Liaw: *Mater. Sci. Eng. A*, 2005, vol. 408, pp. 72–78.
20. M.R. Barnett, M.D. Nave, and C.J. Bettles: *Mater. Sci. Eng. A*, 2004, vol. 386, pp. 205–11.
21. R.D. Field, K.T. Hartwig, C.T. Necher, J.F. Bingert, and S.R. Agnew: *Metall. Mater. Trans. A*, 2002, vol. 23A, pp. 965–72.
22. J.F.W. Bishop and R. Hill: *Philos. Mag.*, 1951, vol. 42, pp. 414–27.
23. R.A. Lebensohn and C.N. Tome: *Acta Metall. Mater.*, 1993, vol. 41, pp. 2611–24.
24. C.N. Tome, R.A. Lebensohn, and U.F. Kocks: *Acta Metall. Mater.*, 1991, vol. 39, pp. 2667–80.
25. H. Watanabe, K. Moriwaki, T. Mukai, T. Ohsuna, K. Hiraga, and K. Higashi: *Mater. Trans. JIM*, 2003, vol. 44, pp. 775–81.
26. T. Obara, H. Yoshinaga, and S. Morozumi: *Acta Metall.*, 1973, vol. 21, pp. 845–53.
27. J.F. Stohr and J.P. Poirier: *Philos. Mag.*, 1972, vol. 25, pp. 1313–29.
28. M.H. Yoo, J.R. Morris, K.M. Ho, and S.R. Agnew: *Metall. Mater. Trans. A*, 2002, vol. 33A, pp. 813–22.
29. J. Koike, T. Kobayashi, T. Mukai, H. Watanabe, M. Suzuki, K. Maruyama, and K. Higashi: *Acta Mater.*, 2003, vol. 51, pp. 2055–65.
30. D.J. Bacon and M.H. Liang: *Phil. Mag. A*, 1986, vol. 53, p. 181.
31. J.R. Morris, J. Scharff, K.M. Ho, and D.E. Turner: *Phil. Mag. A*, 1997, vol. 76, pp. 1065–77.
32. Y. Minonishi, S. Ishioka, S. Morozumi, M. Koiwa, and M. Yamaguchi: *Phil. Mag. A*, 1981, vol. 43, p. 1017.
33. S.R. Agnew, J.A. Horton, and M.H. Yoo: *Metall. Mater. Trans. A*, 2002, vol. 33A, pp. 851–58.
34. A. Galiyev, R. Kaibyshev, and G. Gottstein: *Acta Mater.*, 2001, vol. 49, pp. 1199–1207.
35. U.F. Kocks and H. Mecking: *Progr. Mater. Sci.*, 2003, vol. 48, pp. 171–273.
36. V. Vitek: *Phil. Mag.*, 1968, vol. 18, pp. 773–85.